arXiv:2610.28814v1 [cs.RO] 20 Oct 2026

T-WLA: Bridging Slow Vision and Fast Touch

Kaichen Zhou[1,2,*] **Yuzhen Chen**[2,*] **Hannah Yao**[3,*]
Chonghe Jiang[1] **Rao Fu**[4] **Xihang Yu**[1] **Wei Dai**[1]
Bashar Kabbarah[4] **Haoyu Chen**[2] **Ishita Goluguri**[1] **Zhiyang Dou**[1]
Haonan Chen[2] **Fangneng Zhan**[1] **Mengyu Wang**[2]
Wojciech Matusik[1] **Antonio Torralba**[1] **Paul Pu Liang**[1]

[1]Massachusetts Institute of Technology [2]Harvard University
[3]University of California, Davis [4]University of California, Berkeley
[*]Equal contribution

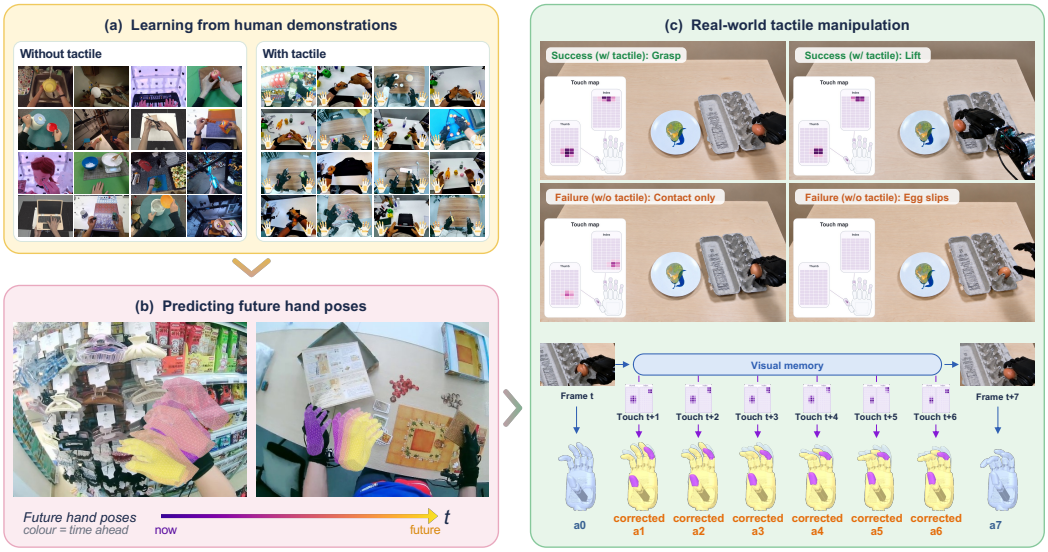


Figure 1: **Tactile World–Language–Action (T-WLA).** The visual branch uses current and past visual information to produce an action chunk and visual memory. Between visual updates, the tactile editor uses this cached visual memory and recent touch to correct the action chunk. During training, predicting future images and pressure helps the model learn features useful for control.

Abstract

In contact-rich manipulation, contact conditions can change before a visual policy updates its action plan. Recomputing the plan through the visual policy adds latency, while tactile feedback alone does not specify how the ongoing motion should be revised for the task. We introduce T-WLA, a world–language–action architecture that uses shared visual memory to guide both action generation and tactile correction. At each visual update, the visual branch integrates the current image, task instruction, and retrieved history into a visual memory that conditions base-action generation. The same memory is cached for a lightweight tactile editor, which combines it with the active action chunk and incoming touch to predict residual corrections to unexecuted actions without rerunning the visual branch. Future-image and future-pressure prediction provide training-only supervision, encouraging the visual memory and tactile features to capture interaction dynamics relevant to action generation and correction. We evaluate T-WLA on tactile-conditioned hand-motion prediction using EgoTouch and Tachin, and on four real-world dexterous manipulation tasks. T-WLA reduces finger-joint MPJPE by 30% relative to the strongest reported baseline and achieves an average success rate of approximately 50.0% across real-robot manipulation tasks. Videos and codes are available at the project website.

Keywords: Robot foundation models; Vision–language–action models (VLA); World-action models (WAM); Visuotactile Manipulation; Residual Action Correction.

1 INTRODUCTION

Contact-rich manipulation refers to tasks whose success depends on precisely managing physical contact with objects or the surrounding environment (Hogan, 2022; Lee et al., 2019). Tactile feedback complements vision by revealing local contact conditions that are difficult to infer from images alone (Niu et al., 2026; Song et al., 2025; Xue et al., 2025; Zhou et al., 2026b). For example, when inserting a plug into a socket, vision guides alignment and approach, while touch provides feedback on contact and insertion resistance. Because these conditions can change between visual updates, tactile feedback supports rapid corrections to the ongoing motion.

Despite the importance of tactile feedback in contact-rich manipulation, many general-purpose robot policies rely primarily on vision. Vision–language–action (VLA) models adapt pretrained vision–language backbones to predict robot actions from visual observations and language instructions (Kim et al., 2024; Physical Intelligence et al., 2025). World–action models further integrate future-state prediction with action generation, linking control decisions to the anticipated evolution of the environment (Zhang et al., 2026b; Yuan et al., 2026). Without tactile feedback, these models must infer local contact conditions from visual cues, which may limit their response to visually subtle contact changes during precise manipulation.

Recent work incorporates tactile feedback into robot control through variable-rate expert architectures (Niu et al., 2026), residual adaptation (Wang et al., 2026), and inference-time policy steering (Wu et al., 2026b). We investigate a complementary question: *how can fast tactile feedback correct a slow visual policy between visual updates?* Our central idea is to generate asynchronous tactile corrections conditioned on persistent visual memory. The visual branch processes RGB observations at 39.7 Hz, producing a base action chunk and a history-aware visual memory at each update. The tactile branch processes touch at 119.1 Hz, combining recent tactile context with the cached visual memory and the active action chunk to predict residual corrections to its remaining, unexecuted actions. This allows contact feedback to refine ongoing motion without waiting for the next visual update or rerunning the visual branch.

We instantiate this idea in T-WLA, a multi-rate architecture for asynchronous visual–tactile control (Fig. 1). The visual branch generates an action chunk and a history-aware visual representation, which is cached until the next visual update. Between these updates, a lightweight tactile editor combines the cached representation with recent tactile observations to produce high-frequency residual corrections to the ongoing action chunk. This separation allows the controller to respond to changing contact conditions without repeatedly running the visual branch. During training, future-image and future-pressure prediction regularize the control representations, encouraging them to capture information relevant to subsequent interactions. Our contributions are summarized as follows:

- **Memory-guided asynchronous control.** We propose T-WLA, which uses the same history-aware visual memory to guide base-action generation and tactile correction. A lightweight tactile editor uses this memory and the active action chunk to correct unexecuted actions between visual updates, without rerunning the visual branch.
- **Predictive supervision for control.** We regularize the visual memory through future-image prediction and the tactile features through both future-image and future-pressure prediction. These auxiliary objectives complement action supervision, and their prediction heads are removed at inference.
- **Evaluation across hand-motion prediction and robot manipulation.** Experiments on EgoTouch and Tachin show improved finger-joint prediction accuracy, while real-robot tests show that T-WLA increases mean task success from 17.0% to 50.0%. Ablations examine the contributions of tactile input, visual history, and predictive supervision.

2 Related work

2.1 Memory and Action Chunk Execution

A single observation may not provide enough information to determine the next action. Memory-based policies address this limitation by retaining information from earlier observations; for example, MemoryVLA stores consolidated perceptual and cognitive entries that can be queried over long horizons (Shi et al., 2026). A complementary line of work predicts temporally extended action sequences. ACT introduced transformer-based action chunking to reduce the effective decision horizon (Zhao et al., 2023), while generative policies such as Diffusion Policy, RDT-1B, and π_0 generate multi-step actions with diffusion or flow-based objectives (Chi et al., 2025; Liu et al., 2025a; Black et al., 2024a). Such temporal coherence can reduce responsiveness when new observations arrive during execution (Liu et al., 2025b; Zeng et al., 2026). Bidirectional Decoding improves closed-loop adaptation by selecting among candidate chunks (Liu et al., 2025b), while Consistency Policy and Streaming Diffusion Policy accelerate generative action synthesis (Prasad et al., 2024; Høeg et al., 2025). Real-time chunking instead explicitly accounts for inference latency when transitioning between successive chunks (Black et al., 2025). T-WLA addresses a complementary setting: it retains visual history across policy updates and uses high-rate tactile feedback to revise the unexecuted portion of an active action chunk.

2.2 Tactile Foundation Models

Tactile representation learning aims to produce features that transfer across sensors and tasks (Bi et al., 2026a; Tao et al., 2026; Heng et al., 2025; Zhang et al., 2026c; Huang et al., 2025). Heterogeneous Tactile Transformer learns a shared model across sensor types (Bi et al., 2026b), while FG-CLTP aligns tactile features with visual and language representations (Ma et al., 2026). Other work explores transferring representations learned from human tactile recordings to dexterous robots (Zhang et al., 2026a) and scaling pretraining through tactile foundation models (Team et al., 2026; Zhou et al., 2026b). Our tactile encoder follows this direction through contrastive pretraining on synchronized tactile and hand-pose histories. Building on tactile representations, several systems study how to incorporate touch into manipulation policies. Multi-rate architectures allow tactile feedback to influence control between visual updates. T-Rex assigns vision and touch to experts operating at different rates (Niu et al., 2026), while Reactive Diffusion Policy combines a slow visual diffusion policy with a fast latent tactile controller (Xue et al., 2025). FA-RDP adapts this division to task demand (Zhuo et al., 2026), and DSWAM organizes world–action modeling into cooperating slow and fast systems (Zhu et al., 2026). Residual adaptation provides another mechanism for incorporating touch into existing policies. ViTaR attaches a lightweight visuotactile residual branch to a frozen backbone (Wang et al., 2026), while ResTacVLA applies residual adaptation in feature space (Zhang et al., 2026d). Tactile feedback can also guide action execution through inference-time adaptation. FBFM introduces asynchronous feedback during flow-matching execution without additional training (Li et al., 2026), while inference-time policy steering adjusts a fixed policy using vision and touch (Wu et al., 2026b). Complementary approaches use touch as training supervision without requiring tactile input at deployment (Gubernatorov et al., 2026; Cheng et al., 2026). These approaches enable tactile feedback to influence action generation and execution. In T-WLA, a cached, history-aware visual representation connects a slow visual policy to a fast tactile editor, which combines visual memory with recent touch to refine the ongoing action chunk. Predictive supervision encourages these representations to capture evolving interaction dynamics, while auxiliary predictors are used only during training and add no inference cost.

3 Methodology

3.1 Overview

During contact-rich manipulation, high frequency changes in contact pressure or location may require the robot to adjust its motion before the next visual update. Tactile feedback captures these local changes, but deciding how to respond also depends on the task instruction and visual information about the ongoing interaction. To retain this information between visual updates, T-WLA shares a history-aware visual memory between a visual policy and a lightweight tactile editor. The

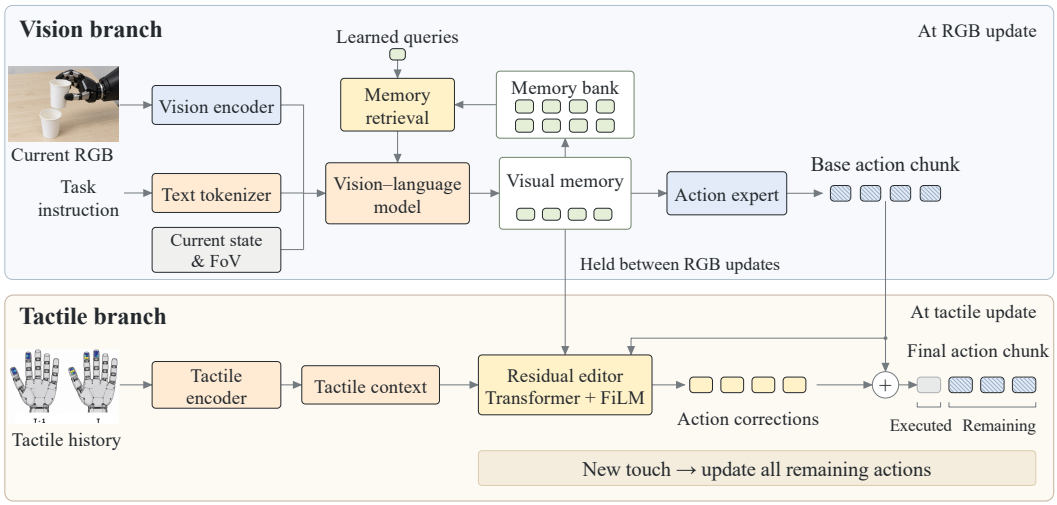


Figure 2: **Shared memory connects slow visual planning with fast tactile correction.** Each visual update generates a base action chunk and visual memory. Between updates, the tactile editor reads this cached pair and revises unexecuted actions without rerunning the visual branch.

editor combines this cached memory with recent tactile observations to asynchronously correct the remaining actions planned by the visual policy, avoiding the computational cost of rerunning the visual branch. As shown in Fig. 2, T-WLA processes RGB observations I_t and higher-frequency tactile observations $T_{t,\tau}$, where t indexes visual updates and τ indexes tactile updates between them. At each visual update, the visual branch produces memory M_{V}^t and an H-step base action chunk $A_t^{\mathrm{base}} = f_{\mathrm{act}}(M_{\mathrm{V}}^t)$. Both are cached while the tactile editor updates the remaining actions:

$$\widehat{A}_{t,\tau} = f_{\mathrm{act}}\left(M_{\mathrm{V}}^t\right) + \mathcal{E}\left(M_{\mathrm{V}}^t, A_t^{\mathrm{base}}, Z_{t,\tau}, \Delta t_{t,\tau}\right). \tag{1}$$

Shared visual memory · Tactile context · Base-action generation · Tactile editor · Cached base action chunk · Elapsed time

Here, $Z_{t,\tau}$ summarizes recent tactile history, $\Delta t_{t,\tau}$ is the elapsed time since current active chunk started, and $\mathcal{E}$ returns an effective residual $\Delta A_{t,\tau}$ for valid, unexecuted actions. The base chunk is sampled once per visual update; each correction is recomputed relative to this cached action chunk.

3.2 History-Aware Visual Memory

A current image may obscure information that was visible earlier or leave the recent approach to contact ambiguous (Wang et al., 2025; Zhou et al., 2026c; 2023). We retain a compact visual history so that both planning and correction can use earlier observations without repeatedly encoding the full image sequence. As illustrated in Fig. 3(a), learned queries Q_{V} retrieve input memory from a bank $\mathcal{B}_{\mathrm{V}}^{t-1}$ containing the last K sets of visual output-memory tokens:

$$M_{\mathrm{V,in}}^t = \mathcal{M}_{\mathrm{V}}\left(\mathcal{B}_{\mathrm{V}}^{t-1}, Q_{\mathrm{V}}\right). \tag{2}$$

The visual backbone then combines this history with current image tokens E_t, instruction tokens L_ℓ, field-of-view tokens c_t, and state tokens S_t:

$$M_{\mathrm{V}}^t = f_{\mathrm{V}}\left(E_t, L_\ell, c_t, S_t, M_{\mathrm{V,in}}^t\right). \tag{3}$$

The updated visual memory M_{V}^t conditions the action expert f_{act} in Eq. 1. The bank update $\mathcal{B}_{\mathrm{V}}^t = \mathrm{Append}_K(\mathcal{B}_{\mathrm{V}}^{t-1}, M_{\mathrm{V}}^t)$ appends the new memory while retaining at most the K most recent memory sets. The tactile editor uses the updated visual memory M_{V}^t, which combines visual history with the current observation and task instruction. The visual branch is trained to predict demonstrated action chunks using conditional flow matching (Lipman et al., 2022), with future-image prediction providing auxiliary supervision in Section 3.4. Details are specified in Appendix B.1 and C.1.

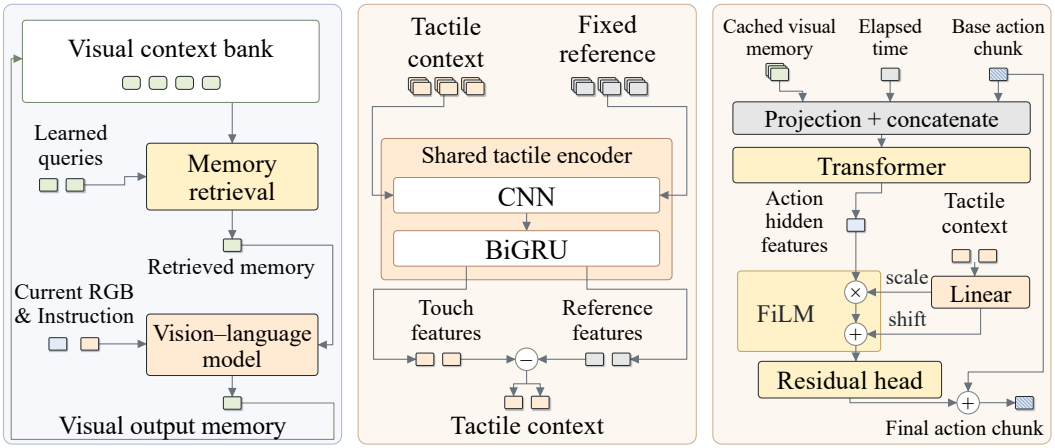


Figure 3: **The memory-to-editor interface.** (a) Retrieved history is combined with the current observation and instruction. (b) Observed tactile history is encoded relative to a fixed reference. (c) Touch modulates action features conditioned on the cached visual memory, base chunk, and elapsed time. Module details are in Appendices B.1–B.3.

3.3 Asynchronous Tactile Correction

The editor asynchronously refines an active plan through residual corrections rather than generating a new action plan from touch alone. Visual memory supplies retained task and scene information; the base action chunk specifies what is being executed; and elapsed time identifies the remaining action positions as in Eq. 1. Between visual updates, M_{V}^{t} and A_{t}^{base} remain fixed, while each tactile update τ runs only the lightweight tactile encoder and residual editor, enabling efficient corrections without rerunning the visual branch. This formulation assumes that the base plan remains a useful reference between visual updates.

Tactile context. We encode recent causally available tactile frames $\mathcal{H}_{t,\tau}$ as $Z_{t,\tau} = \mathrm{Enc}_{\mathrm{T}}(\mathcal{H}_{t,\tau})$. A temporal window exposes contact evolution that a single pressure map cannot resolve. Figure 3(b) shows the shared encoder and reference subtraction; more information are detailed in Appendix B.2.

Plan-conditioned correction. As illustrated in Fig. 3(c), a small Transformer combines the cached visual memory, base action chunk, and elapsed time to produce action features at each tactile update. FiLM (Perez et al., 2018) uses the tactile context to scale and shift these features, which a residual head converts into action corrections. After masking, the corrections $\Delta A_{t,\tau}$ affect only valid, unexecuted actions; a hand with missing tactile input receives zero correction. The residual is added to the original cached base action chunk, yielding $\widehat{A}_{t,\tau} = A_{t}^{\mathrm{base}} + \Delta A_{t,\tau}$ as in Eq. 1, rather than accumulated on previously corrected actions. More structure details are provided in Appendix B.3. With the visual branch frozen, we supervise the corrected actions using a group-balanced Smooth L1 loss against demonstrations and regularize the predicted residuals with a magnitude penalty. These objectives train the tactile encoder and residual editor to correct action errors while discouraging unnecessarily large corrections. Definitions of objectives are provided in Appendix C.1.

3.4 Predictive Supervision and Training

Action supervision specifies the demonstrated command, but may not distinguish states with different subsequent visual or contact outcomes. We add future-image and future-pressure prediction to supervise information about these outcomes in the representations used for control. Both prediction heads are training-only auxiliaries, not inference-time planners.

Complementary prediction targets. The image predictor conditions on current image tokens and output visual memory to predict future latents supplied by a frozen image encoder. During editor training, tactile context also conditions this predictor through a learned adapter. The adapter changes only the auxiliary prediction path, leaving the cached memory used for control unchanged. Future-

Table 1: Tactile-conditioned future hand-motion prediction. EgoTouch is reported across five native environments and as a macro-average; Tachin is evaluated on its held-out test split. Metrics use the same prediction horizon and are averaged per sequence before aggregation. Lower prediction error is better. Gray highlights T-WLA. **Bold**/underline indicate the best/second-best distinct reported errors within each metric and column, including ties. Tactile Freq. denotes the effective tactile-correction rate under our multi-rate protocol. Frequency is reported in Hz and is not ranked.

	EgoTouch						Tachin	
Method	Home	Workb.	Office	Retail	Outdoor	Avg.	Overall	Tactile Freq.
Wrist translation error (cm, ↓)								
VITRA + tactile	4.54	3.71	2.84	3.98	5.34	4.08	1.48	58.2
SmolVLA + tactile	4.55	3.74	2.88	3.98	5.33	4.10	1.50	69.0
MemoryVLA + tactile	4.65	3.78	2.96	4.08	5.41	4.18	1.55	15.0
T-Rex	4.63	3.76	2.95	4.05	5.41	4.16	1.54	17.16
T-WLA	**4.36**	**3.63**	**2.73**	**3.82**	**5.24**	**3.96**	**1.39**	**119.1**
Wrist rotation geodesic error (degrees, ↓)								
VITRA + tactile	6.29	6.22	4.81	6.86	7.15	6.27	4.55	58.2
SmolVLA + tactile	6.29	6.22	4.87	6.85	7.16	6.28	4.20	69.0
MemoryVLA + tactile	6.34	6.39	4.88	6.89	7.20	6.34	4.39	15.0
T-Rex	6.29	6.29	4.84	6.87	7.17	6.29	4.25	17.16
T-WLA	**6.18**	**5.83**	**4.79**	**6.66**	**7.03**	**6.10**	**4.17**	**119.1**
Wrist-relative finger-joint MPJPE (cm, ↓)								
VITRA + tactile	0.51	0.51	0.45	0.51	0.53	0.50	0.63	58.2
SmolVLA + tactile	0.51	0.50	0.46	0.50	0.53	0.50	1.28	69.0
MemoryVLA + tactile	1.37	1.37	1.17	1.34	1.46	1.34	1.87	15.0
T-Rex	1.17	1.13	1.07	1.17	1.18	1.14	1.08	17.16
T-WLA	**0.36**	**0.33**	**0.31**	**0.36**	**0.40**	**0.35**	**0.46**	**119.1**

pressure prediction instead supervises subsequent contact, conditioned on visual memory, tactile context, and upcoming edited actions. This action condition links tactile features to how contact may evolve under the active plan. Predictor conditions, gradient routes, and normalization are specified in Appendix C.2; future targets never enter the controller.

Staged optimization. The visual action expert and predictive heads use conditional flow matching (Lipman et al., 2022). We first train the visual branch with action and image-prediction supervision, and separately pretrain the tactile encoder through contrastive learning on synchronized tactile and hand-pose histories from EgoTouch. We then freeze the visual branch and use its cached visual memory and base action chunks to train the tactile encoder and residual editor with a group-balanced Smooth L1 action loss, a residual-magnitude penalty, and the two predictive objectives. The visual predictor remains frozen, while its tactile conditioning adapter and the pressure predictor are trained. Objective definitions and custom reductions are provided in Appendices C.1 and C.2. Stage-specific training details and a proposed joint fine-tuning extension are described in Appendix C.3. Both prediction heads are removed at inference.

4 Experiments

We organize our experiments around four questions. First, does combining visual memory with high-rate tactile feedback improve future hand-motion prediction on human-interaction datasets (Section 4.2)? Second, does the tactile branch improve closed-loop success on real contact-rich robot tasks under a matched visual backbone and training budget (Section 4.3)? Third, which components—tactile input, recurrent memory, memory capacity, and predictive supervision—account for the improvement (Section 4.4)? Finally, does the visual branch remain a strong standalone predictor when tactile observations are unavailable (Appendix E)?

4.1 Experimental Setup

Datasets and tasks. For tactile-conditioned future hand-motion prediction, we evaluate on EgoTouch from TouchAnything (Zhou et al., 2026a) and the Tachin glove dataset (Tachintech, 2026). EgoTouch is evaluated in its five native environments—Home, Workbench, Office, Retail, and Outdoor—whereas Tachin is reported over its complete held-out test set. For visual-only predic-

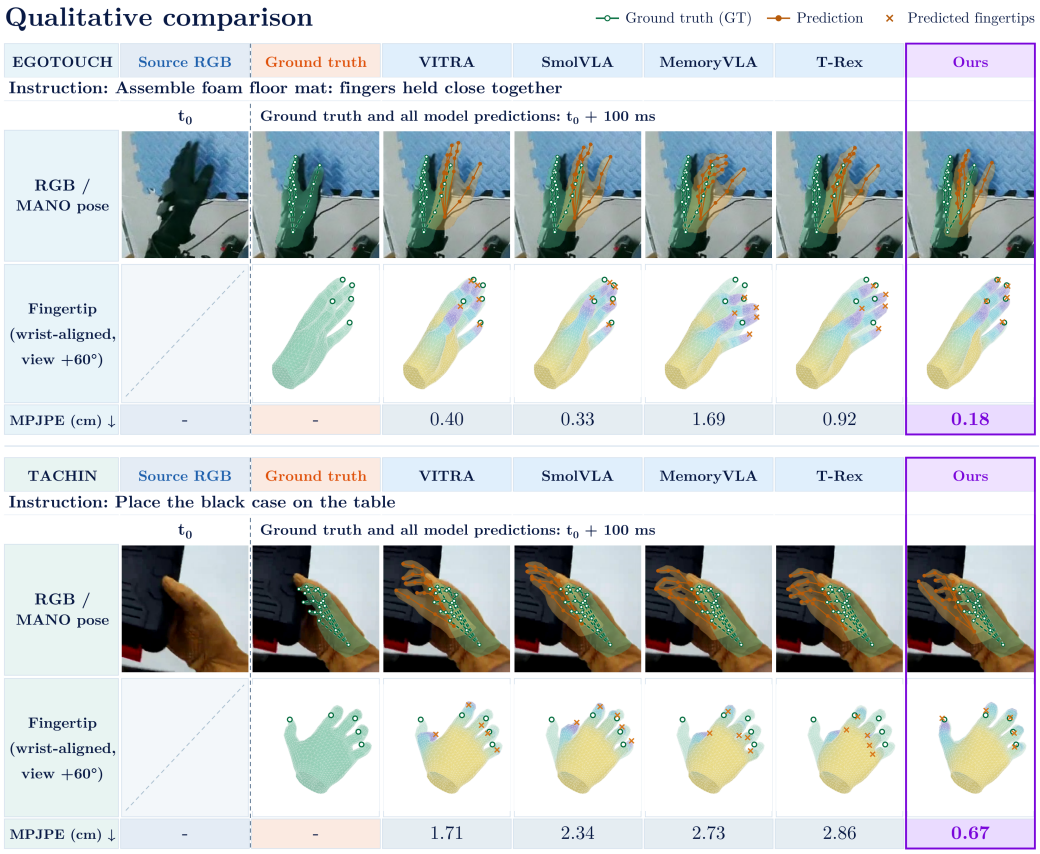


Figure 4: **Qualitative comparison on EgoTouch and Tachin.** VITRA, SmolVLA, MemoryVLA, and T-Rex denote the tactile-augmented variants used in Table 1. For each dataset, we show the source RGB frame at t_0, ground truth, and predictions from each of the models at $t_0 + 100\,\text{ms}$. RGB overlays depict ground-truth hand poses in green and predictions in orange. Fingertip-detail views show wrist-aligned hands rendered from a $+60°$ visualization view, with ground-truth hand mesh in green and predicted fingertips in orange crosses. MPJPE is reported in centimeters (↓: lower is better). T-WLA obtains the lowest MPJPE on both displayed examples.

tion, we use GigaHands (Fu et al., 2025), OakInk2 (Zhan et al., 2024), and TACO (Liu et al., 2024). GigaHands is reported over its five official activity families, while OakInk2 and TACO are each evaluated over their complete held-out test sets. Our real-robot benchmark contains four contact-rich tasks: egg handling, single-sheet pickup, paper-cup nesting, and paper-bag opening.

Baselines and controlled comparison. For tactile-conditioned prediction, we compare with VITRA (Li et al., 2025), SmolVLA (Shukor et al., 2025), MemoryVLA (Shi et al., 2026), and T-Rex (Niu et al., 2026). When a baseline does not natively accept touch, its "+ tactile" variant receives the same synchronized tactile stream and uses the same task-specific tactile encoder, prediction head, and optimization budget as the other adapted baselines. T-Rex and T-WLA retain their native multi-rate interfaces. Appendix D specifies the action representation, temporal alignment, metric definitions, evaluation masks, and aggregation procedure.

4.2 Tactile- and Vision-Conditioned Action Prediction

Tactile-conditioned hand-motion prediction. Table 1 shows that T-WLA achieves the lowest reported errors across all three metrics in every EgoTouch environment and on Tachin. The clearest advantage, however, is in finger articulation: wrist-relative MPJPE decreases by approximately 30.0% on EgoTouch and 27.0% on Tachin relative to the strongest reported baseline for each dataset. Because this metric measures joint positions relative to the wrist, the improvement is not simply a

Table 2: Closed-loop success rates (%, ↑) on four contact-rich robot tasks after adaptation with 30 teleoperated demonstrations per task. Avg. denotes the unweighted mean across tasks. **Bold**/underline indicate the best/second-best distinct results in each column, including ties. Gray highlights tactile-enabled T-WLA.

Controller	Egg Transfer	Single-Sheet Pickup	Paper-Cup Nesting	Paper-Bag Dragging	Avg.
SmolVLA	0	28	0	39	16.75
SmolVLA + Tactile	0	30	1	37	17.0
T-ReX	4	3	**22**	63	23.0
T-WLA w/o tactile	18	72	17	82	47.25
T-WLA	**21**	**78**	17	**84**	**50.0**

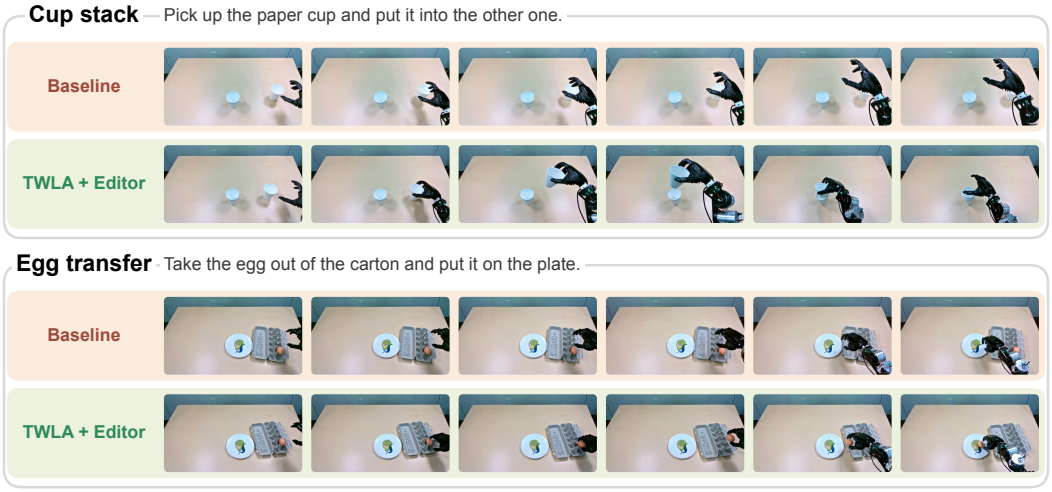


Figure 5: Representative real-robot trials for cup stack and egg transfer. Each column shows the start, contact, and goal frames of one episode; the left column of each task is a successful T-WLA trial and the right column is a failed baseline trial.

consequence of predicting the global wrist position more accurately. Wrist translation and rotation also improve, but more modestly. This contrast is consistent with the intended role of the tactile editor: refining fine-grained hand motion within an ongoing visual plan, rather than replacing the plan altogether. The same pattern across both datasets, together with lower errors in all five EgoTouch environments, indicates that the benefit is not confined to a single environment. The accuracy improvements also coexist with a higher effective tactile-correction rate. Under our multi-rate protocol, T-WLA reaches 119.1 Hz, compared with 69.0 Hz for the fastest reported baseline. Thus, the lightweight correction pathway combines more frequent tactile updates with lower prediction errors, rather than requiring a lower update rate to obtain better predictions. This accuracy–update-rate combination is particularly relevant to asynchronous visuotactile control, where contact-driven corrections are needed between slower visual updates.

4.3 Real-Robot Evaluation

Next, we test whether the prediction improvements translate into closed-loop manipulation on four tasks: egg transfer, single-sheet pickup, paper-cup nesting, and paper-bag dragging. These tasks are contact-sensitive: egg transfer involves small in-hand slip that is difficult to observe visually; sheet pickup and cup nesting require a secure grip without crumpling or crushing the object; and bag dragging requires maintaining a grasp on the loaded bag's rim under changing fingertip loads. Together, they test whether tactile feedback can refine visually guided actions using contact information that images alone may not resolve. As shown in Table 2, T-WLA with tactile input achieves a mean success rate of 50.0% with only 30 teleoperated demonstrations per task. Before robot adaptation, T-WLA, including its tactile editor, is trained only on human-hand data. Even without tactile input, T-WLA reaches 47.25% mean success, compared with 16.75% for SmolVLA, which shares components with our visual branch. VITRA and MemoryVLA achieve no successful trials under

Table 3: Ablation of tactile input, memory, and predictive supervision. World-prediction ablations remove auxiliary objectives during editor training, not backbone pretraining. Lower is better for every metric. **Bold**/underline indicate the best/second-best distinct results in each column.

	EgoTouch			Tachin		
Variant	Trans. (cm)	Rot. (°)	Joint (cm)	Trans. (cm)	Rot. (°)	Joint (cm)
Without tactile input	4.010	6.200	0.430	1.450	4.400	0.500
Without recurrent memory	4.070	6.280	0.370	1.690	4.560	0.490
Shorter memory ($K_{\text{short}} < K$)	3.980	6.150	0.360	1.480	4.310	**0.460**
Without world prediction (T+V)	3.963	6.113	0.353	1.413	4.283	0.463
Without world prediction (T)	<u>3.962</u>	<u>6.112</u>	<u>0.352</u>	<u>1.412</u>	<u>4.263</u>	<u>0.462</u>
Without world prediction (V)	3.963	6.113	0.353	1.423	4.273	0.463
T-WLA	**3.960**	**6.100**	**0.350**	**1.390**	**4.170**	**0.460**

the same demonstration budget. These closed-loop results complement the finger-motion prediction improvements in Table 1. The benefit of tactile input varies across tasks, with the largest gain in single-sheet pickup (6 percentage points). A thin sheet requires a precise pinch with enough force to prevent slipping but not enough to crumple it, so this improvement is consistent with tactile feedback helping regulate a delicate grasp. The smaller gains in egg transfer and bag dragging may similarly reflect the value of sensing changes in grasp stability and fingertip load. Cup nesting, however, remains at 17%: maintaining a secure grasp without crushing the cup addresses only part of the task, which also requires correct alignment and placement. Grip-related corrections may be insufficient if failures occur during these other stages, although the aggregate success rate does not identify the limiting stage. In observed SmolVLA failures, the hand often closes away from the target, leaving little contact feedback to guide a correction. This may explain its smaller tactile gain when the base action fails to establish contact.

4.4 Ablation Studies

Table 3 isolates the effects of tactile input, recurrent history, memory capacity, and predictive supervision under matched settings. Removing tactile input produces the largest increase in finger-joint error on both datasets: 22.9% on EgoTouch and 8.7% on Tachin. Translation and rotation errors also increase by 1.3% and 1.6% on EgoTouch, and by 4.3% and 5.5% on Tachin. Removing recurrent memory has a larger effect on wrist prediction, particularly on Tachin, where translation and rotation errors increase by 21.6% and 9.4%. Shortening memory from $K = 8$ to $K_{\text{short}} = 4$ increases error by 2.3% on average across the six metrics, while removing both world-prediction objectives increases it by 1.0% on the same basis. The full T-WLA achieves the lowest error in five of six metrics and ties for the lowest Tachin joint error.

5 Conclusion

We presented T-WLA, a multi-rate visuotactile architecture that caches history-aware visual memory to guide high-frequency tactile corrections. A slow visual policy generates base action chunks, while a lightweight tactile editor reuses the cached visual memory to refine ongoing actions at a higher frequency. Future-image and future-pressure prediction regularize the control representations during training, complementing action supervision with interaction dynamics. Extensive results show that joint visual-tactile modeling and predictive supervision improve contact-rich manipulation.

REFERENCES

Jianxin Bi, Kevin Yuchen Ma, Ce Hao, Mike Shou Zheng, and Harold Soh. Vla-touch: Enhancing vision-language-action model with dual-level tactile feedback. *IEEE Robotics and Automation Letters*, 2026a.

Jianxin Bi, Qiang Wang, Jayaram Reddy, Kelvin Lin, Soibkhon Khajikhanov, Ruihan Gao, and Harold Soh. Heterogeneous tactile transformer. *arXiv preprint arXiv:2606.29948*, 2026b.

Johan Bjorck, Fernando Castañeda, Nikita Cherniadev, Xingye Da, Runyu Ding, Linxi Fan, Yu Fang, Dieter Fox, Fengyuan Hu, Spencer Huang, et al. Gr00t n1: An open foundation model for generalist humanoid robots. *arXiv preprint arXiv:2503.14734*, 2025.

Kevin Black, Noah Brown, Danny Driess, Adnan Esmail, Michael Equi, Chelsea Finn, Niccolo Fusai, Lachy Groom, Karol Hausman, Brian Ichter, Szymon Jakubczak, Tim Jones, Liyiming Ke, Sergey Levine, Adrian Li-Bell, Mohith Mothukuri, Suraj Nair, Karl Pertsch, Lucy Xiaoyang Shi, James Tanner, Quan Vuong, Anna Walling, Haohuan Wang, and Ury Zhilinsky. π_0: A Vision-Language-Action Flow Model for General Robot Control. *arXiv preprint arXiv:2410.24164*, 2024a.

Kevin Black, Noah Brown, Danny Driess, Adnan Esmail, Michael Equi, Chelsea Finn, Niccolo Fusai, Lachy Groom, Karol Hausman, Brian Ichter, et al. π_0: A vision-language-action flow model for general robot control. *arXiv preprint arXiv:2410.24164*, 2024b.

Kevin Black, Manuel Galliker, and Sergey Levine. Real-Time Execution of Action Chunking Flow Policies. In *Advances in Neural Information Processing Systems*, volume 38, 2025. doi: 10.52202/085713-1122.

Anthony Brohan, Noah Brown, Justice Carbajal, Yevgen Chebotar, Joseph Dabis, Chelsea Finn, Keerthana Gopalakrishnan, Karol Hausman, Alex Herzog, Jasmine Hsu, et al. Rt-1: Robotics transformer for real-world control at scale. *arXiv preprint arXiv:2212.06817*, 2022.

Anthony Brohan, Noah Brown, Justice Carbajal, Yevgen Chebotar, Xi Chen, Krzysztof Choromanski, Tianli Ding, Danny Driess, Avinava Dubey, Chelsea Finn, et al. Rt-2: Vision-language-action models transfer web knowledge to robotic control. *arXiv preprint arXiv:2307.15818*, 2023.

Ning Cheng, Jinan Xu, Wanlin Li, Yangzhi Chen, Jing Gao, Yiqun Wang, Kelan Peng, and Wenjuan Han. τ: Learning Touch-Augmented Vision-Language-Action Models from Future Visual Supervision. *arXiv preprint arXiv:2607.24485*, 2026.

Cheng Chi, Zhenjia Xu, Siyuan Feng, Eric Cousineau, Yilun Du, Benjamin Burchfiel, Russ Tedrake, and Shuran Song. Diffusion policy: Visuomotor policy learning via action diffusion. *The International Journal of Robotics Research*, 44(10-11):1684–1704, 2025.

Danny Driess, Fei Xia, Mehdi SM Sajjadi, Corey Lynch, Aakanksha Chowdhery, Brian Ichter, Ayzaan Wahid, Jonathan Tompson, Quan Vuong, Tianhe Yu, et al. Palm-e: An embodied multimodal language model. *arXiv preprint arXiv:2303.03378*, 2023.

Rao Fu, Dingxi Zhang, Alex Jiang, Wanjia Fu, Austin Funk, Daniel Ritchie, and Srinath Sridhar. Gigahands: A massive annotated dataset of bimanual hand activities. In *2025 IEEE/CVF Conference on Computer Vision and Pattern Recognition (CVPR)*, pp. 17461–17474. IEEE, 2025.

Konstantin Gubernatorov, Mikhail Sannikov, Ilya Mikhalchuk, Egor Kuznetsov, Makar Artemov, Ogunwoye Faith Oluwatobi, Marcelino Fernando, Artem Asanov, Ziang Guo, and Dzmitry Tsetserukou. Hapticvla: Contact-rich manipulation via vision-language-action model without inference-time tactile sensing. *arXiv preprint arXiv:2603.15257*, 2026.

Liang Heng, Haoran Geng, Kaifeng Zhang, Pieter Abbeel, and Jitendra Malik. Vitacformer: Learning cross-modal representation for visuo-tactile dexterous manipulation. *arXiv preprint arXiv:2506.15953*, 2025.

Sigmund Hennum Høeg, Yilun Du, and Olav Egeland. Streaming Diffusion Policy: Fast Policy Synthesis with Variable Noise Diffusion Models. In *2025 IEEE International Conference on Robotics and Automation (ICRA)*. IEEE, 2025.

Neville Hogan. Contact and physical interaction. *Annual Review of Control, Robotics, and Autonomous Systems*, 5(1):179–203, 2022.

Bohan Hou, Gen Li, Jindou Jia, Tuo An, Xinying Guo, Sicong Leng, Haoran Geng, Yanjie Ze, Tatsuya Harada, Philip Torr, et al. World model for robot learning: A comprehensive survey. *arXiv preprint arXiv:2605.00080*, 2026.

Jialei Huang, Shuo Wang, Fanqi Lin, Yihang Hu, Chuan Wen, and Yang Gao. Tactile-vla: unlocking vision-language-action model's physical knowledge for tactile generalization. *arXiv preprint arXiv:2507.09160*, 2025.

Moo Jin Kim, Karl Pertsch, Siddharth Karamcheti, Ted Xiao, Ashwin Balakrishna, Suraj Nair, Rafael Rafailov, Ethan Foster, Grace Lam, Pannag Sanketi, et al. Openvla: An open-source vision-language-action model. *arXiv preprint arXiv:2406.09246*, 2024.

Moo Jin Kim, Chelsea Finn, and Percy Liang. Fine-tuning vision-language-action models: Optimizing speed and success. *arXiv preprint arXiv:2502.19645*, 2025.

Michelle A Lee, Yuke Zhu, Peter Zachares, Matthew Tan, Krishnan Srinivasan, Silvio Savarese, Li Fei-Fei, Animesh Garg, and Jeannette Bohg. Making sense of vision and touch: Learning multimodal representations for contact-rich tasks. *arXiv preprint arXiv:1907.13098*, 2019.

Peize Li, Ruimeng Zhang, Ru Zhang, Cong Huang, Kai Chen, and Shanghang Zhang. Fbfm: A training-free asynchronous feedback mechanism for flow-matching in world-action models execution. *arXiv preprint arXiv:2607.29235*, 2026.

Qixiu Li, Yu Deng, Yaobo Liang, Lin Luo, Lei Zhou, Chengtang Yao, Lingqi Zeng, Zhiyuan Feng, Huizhi Liang, Sicheng Xu, et al. Scalable vision-language-action model pretraining for robotic manipulation with real-life human activity videos. *arXiv preprint arXiv:2510.21571*, 2025.

Yaron Lipman, Ricky TQ Chen, Heli Ben-Hamu, Maximilian Nickel, and Matt Le. Flow matching for generative modeling. *arXiv preprint arXiv:2210.02747*, 2022.

Songming Liu, Lingxuan Wu, Bangguo Li, Hengkai Tan, Huayu Chen, Zhengyi Wang, Ke Xu, Hang Su, and Jun Zhu. Rdt-1b: a diffusion foundation model for bimanual manipulation. In *International Conference on Learning Representations*, volume 2025, pp. 29982–30009, 2025a.

Yuejiang Liu, Jubayer Hamid, Annie Xie, Yoonho Lee, Max Du, and Chelsea Finn. Bidirectional decoding: Improving action chunking via guided test-time sampling. In *International Conference on Learning Representations*, volume 2025, pp. 4594–4627, 2025b.

Yun Liu, Haolin Yang, Xu Si, Ling Liu, Zipeng Li, Yuxiang Zhang, Yebin Liu, and Li Yi. TACO: Benchmarking Generalizable Bimanual Tool-ACtion-Object Understanding. In *Proceedings of the IEEE/CVF Conference on Computer Vision and Pattern Recognition (CVPR)*, pp. 21740–21751, 2024.

Wenxuan Ma, Chaofan Zhang, Yinghao Cai, Guocai Yao, Shaowei Cui, and Shuo Wang. Fg-cltp: Fine-grained contrastive language tactile pretraining for robotic manipulation. *IEEE Robotics and Automation Letters*, 2026.

Dantong Niu, Zhuoyang Liu, Zekai Wang, Boning Shao, Zhao-Heng Yin, Anirudh Pai, Yuvan Sharma, Stefano Saravalle, Ruijie Zheng, Jing Wang, et al. T-rex: Tactile-reactive dexterous manipulation. *arXiv preprint arXiv:2606.17055*, 2026.

Abby O'Neill, Abdul Rehman, Abhiram Maddukuri, Abhishek Gupta, Abhishek Padalkar, Abraham Lee, Acorn Pooley, Agrim Gupta, Ajay Mandlekar, Ajinkya Jain, et al. Open x-embodiment: Robotic learning datasets and rt-x models: Open x-embodiment collaboration 0. In *2024 IEEE International Conference on Robotics and Automation (ICRA)*, pp. 6892–6903. IEEE, 2024.

Ethan Perez, Florian Strub, Harm De Vries, Vincent Dumoulin, and Aaron Courville. Film: Visual reasoning with a general conditioning layer. In *Proceedings of the AAAI conference on artificial intelligence*, volume 32, 2018.

Karl Pertsch, Kyle Stachowicz, Brian Ichter, Danny Driess, Suraj Nair, Quan Vuong, Oier Mees, Chelsea Finn, and Sergey Levine. Fast: Efficient action tokenization for vision-language-action models. *arXiv preprint arXiv:2501.09747*, 2025.

Physical Intelligence, Kevin Black, Noah Brown, James Darpinian, Karan Dhabalia, Danny Driess, Adnan Esmail, Michael Equi, Chelsea Finn, Niccolo Fusai, et al. pi0.5: A Vision-Language-Action Model with Open-World Generalization. *arXiv preprint arXiv:2504.16054*, 2025.

Aaditya Prasad, Kevin Lin, Jimmy Wu, Linqi Zhou, and Jeannette Bohg. Consistency Policy: Accelerated Visuomotor Policies via Consistency Distillation. In *Proceedings of Robotics: Science and Systems*, 2024. doi: 10.15607/RSS.2024.XX.071.

Scott Reed, Konrad Zolna, Emilio Parisotto, Sergio Gomez Colmenarejo, Alexander Novikov, Gabriel Barth-Maron, Mai Gimenez, Yury Sulsky, Jackie Kay, Jost Tobias Springenberg, et al. A generalist agent. *arXiv preprint arXiv:2205.06175*, 2022.

Hao Shi, Bin Xie, Yingfei Liu, Lin Sun, Fengrong Liu, Tiancai Wang, Erjin Zhou, Haoqiang Fan, Xiangyu Zhang, and Gao Huang. Memoryvla: Perceptual-cognitive memory in vision-language-action models for robotic manipulation. In *International Conference on Learning Representations*, volume 2026, pp. 18567–18602, 2026.

Mustafa Shukor, Dana Aubakirova, Francesco Capuano, Pepijn Kooijmans, Steven Palma, Adil Zouitine, Michel Aractingi, Caroline Pascal, Martino Russi, Andres Marafioti, et al. Smolvla: A vision-language-action model for affordable and efficient robotics. *arXiv preprint arXiv:2506.01844*, 2025.

Yuxin Ray Song, Jinzhou Li, Rao Fu, Devin Murphy, Kaichen Zhou, Rishi Shiv, Yaqi Li, Haoyu Xiong, Crystal Elaine Owens, Yilun Du, et al. Opentouch: Bringing full-hand touch to real-world interaction. *arXiv preprint arXiv:2512.16842*, 2025.

Tachintech. TachinTactileGlove-Demo01. Hugging Face dataset, 2026. Accessed September 23, 2026.

Zhengyu Tao, Xin Li, and Xin Wang. Foretac-vla: A forecasting-based tactile-vision-language-action model for contact-rich robotic manipulation. *arXiv preprint arXiv:2609.20980*, 2026.

Gemini Robotics Team, Saminda Abeyruwan, Joshua Ainslie, Jean-Baptiste Alayrac, Montserrat Gonzalez Arenas, Travis Armstrong, Ashwin Balakrishna, Robert Baruch, Maria Bauza, Michiel Blokzijl, et al. Gemini robotics: Bringing ai into the physical world. *arXiv preprint arXiv:2503.20020*, 2025.

NeoteAI Team, Fudan TEAI Team, et al. N0-foundation: Towards the age of tactile intelligence, 2026.

Octo Model Team, Dibya Ghosh, Homer Walke, Karl Pertsch, Kevin Black, Oier Mees, Sudeep Dasari, Joey Hejna, Tobias Kreiman, Charles Xu, et al. Octo: An open-source generalist robot policy. *arXiv preprint arXiv:2405.12213*, 2024.

Jianyuan Wang, Minghao Chen, Nikita Karaev, Andrea Vedaldi, Christian Rupprecht, and David Novotny. Vggt: Visual geometry grounded transformer. In *2025 IEEE/CVF Conference on Computer Vision and Pattern Recognition (CVPR)*, pp. 5294–5306. IEEE, 2025.

Yi Wang, Renjun Wu, Jinyan Liu, and Xuesong Li. Vitar: Visuo-tactile residual adaptation for foundation vla manipulation. *arXiv preprint arXiv:2608.15816*, 2026.

Wei Wu, Fan Lu, Yunnan Wang, Shuai Yang, Shi Liu, Fangjing Wang, Qian Zhu, He Sun, Yong Wang, Shuailei Ma, et al. A pragmatic vla foundation model. *arXiv preprint arXiv:2601.18692*, 2026a.

Yilin Wu, Zilin Si, Zeynep Temel, Oliver Kroemer, and Andrea Bajcsy. Inference-time policy steering via vision and touch. *arXiv preprint arXiv:2606.14981*, 2026b.

Han Xue, Jieji Ren, Wendi Chen, Gu Zhang, Yuan Fang, Guoying Gu, Huazhe Xu, and Cewu Lu. Reactive diffusion policy: Slow-fast visual-tactile policy learning for contact-rich manipulation. *arXiv preprint arXiv:2503.02881*, 2025.

Seonghyeon Ye, Yunhao Ge, Kaiyuan Zheng, Shenyuan Gao, Sihyun Yu, George Kurian, Suneel Indupuru, You Liang Tan, Chuning Zhu, Jiannan Xiang, et al. World action models are zero-shot policies. *arXiv preprint arXiv:2602.15922*, 2026a.

Seonghyeon Ye, Yunhao Ge, Kaiyuan Zheng, Shenyuan Gao, Sihyun Yu, George Kurian, Suneel Indupuru, You Liang Tan, Chuning Zhu, Jiannan Xiang, et al. World action models are zero-shot policies. *arXiv preprint arXiv:2602.15922*, 2026b.

Tianyuan Yuan, Zibin Dong, Yicheng Liu, and Hang Zhao. Fast-wam: Do world action models need test-time future imagination? *arXiv preprint arXiv:2603.16666*, 2026.

Michael Zeng, Abhinav Agarwal, Ajay Bati, Brian Lee, Siddharth Ancha, and Russ Tedrake. Revisiting open-loop execution in robotics: Toward reactive, higher-performing policies. *arXiv preprint arXiv:2608.15938*, 2026.

Xinyu Zhan, Lixin Yang, Yifei Zhao, Kangrui Mao, Hanlin Xu, Zenan Lin, Kailin Li, and Cewu Lu. Oakink2: A dataset of bimanual hands-object manipulation in complex task completion. In *2024 IEEE/CVF Conference on Computer Vision and Pattern Recognition (CVPR)*, pp. 445–456. IEEE, 2024.

Chi Zhang, Penglin Cai, Ziheng Xi, Haoqi Yuan, Hao Luo, Wanpeng Zhang, Sipeng Zheng, Chaoyi Xu, and Zongqing Lu. Human-centric transferable tactile pre-training for dexterous robotic manipulation. *arXiv preprint arXiv:2607.01067*, 2026a.

Chushan Zhang, Jinguang Tong, Xuesong Li, Yikai Wang, and Hongdong Li. Keep the future, drop the rollout: Rift for world action models. *arXiv preprint arXiv:2608.11521*, 2026b.

Kaidi Zhang, Heng Zhang, Zhengtong Xu, Zhiyuan Zhang, Md Rakibul Islam Prince, Xiang Li, Xiaojing Han, Yuhao Zhou, Arash Ajoudani, and Yu She. Tacvla: Contact-aware tactile fusion for robust vision-language-action manipulation. *arXiv preprint arXiv:2603.12665*, 2026c.

Pengwei Zhang, Bin Xie, Xinpan Meng, Xinyu Guo, Ce Hao, Fang Deng, Long Cheng, and Tiancai Wang. Feeling the unexpected: Restacvla for contact-rich manipulation via residual tactile representation. *arXiv preprint arXiv:2607.03387*, 2026d.

Tony Z. Zhao, Vikash Kumar, Sergey Levine, and Chelsea Finn. Learning Fine-Grained Bimanual Manipulation with Low-Cost Hardware. In *Proceedings of Robotics: Science and Systems*, 2023. doi: 10.15607/RSS.2023.XIX.016.

Ruijie Zheng, Jing Wang, Scott Reed, Johan Björck, Yu Fang, Fengyuan Hu, Joel Jang, Kaushil Kundalia, Zongyu Lin, Loic Magne, Avnish Narayan, You Liang Tan, Guanzhi Wang, Qi Wang, Jiannan Xiang, Yinzhen Xu, Seonghyeon Ye, Jan Kautz, Furong Huang, Yuke Zhu, and Linxi Fan. FLARE: Robot Learning with Implicit World Modeling. In *Conference on Robot Learning (CoRL)*, 2025.

Jianyi Zhou, Ziteng Gao, Feiyang Hong, Zirui Liu, Guannan Zhang, Weisheng Dai, Ruichen Zhen, Chuqiao Lyu, Haotian Wu, Yinian Mao, et al. Touchanything: A dataset and framework for bimanual tactile estimation from egocentric video. *arXiv preprint arXiv:2605.13083*, 2026a.

Jianyi Zhou, Feiyang Hong, Yunhao Li, Yicheng Zhao, Yongjue Cen, Zirui Liu, Jiakang Huang, Zirui Chen, Ruiyang Zhang, Weizhuo Zhu, et al. Touchworld: A predictive and reactive tactile foundation model for dexterous manipulation. *arXiv preprint arXiv:2607.07287*, 2026b.

Kaichen Zhou, Jia-Xing Zhong, Sangyun Shin, Kai Lu, Yiyuan Yang, Andrew Markham, and Niki Trigoni. Dynpoint: Dynamic neural point for view synthesis. *Advances in Neural Information Processing Systems*, 36:69532–69545, 2023.

Kaichen Zhou, Yuhan Wang, Grace Chen, Gaspard Beaudouin, Fangneng Zhan, Paul Liang, and Mengyu Wang. Page-4d: Disentangled pose and geometry estimation for vggt-4d perception. In *International Conference on Learning Representations*, volume 2026, pp. 36401–36414, 2026c.

Jian Zhu, Jianjun Zhang, Taiyi Su, Tianbin Liu, Zhangyuan Wang, Kai Xie, Zitai Huang, Chong Ma, Youzhang He, Tianjian Wang, et al. Dswam: A dual-system world action foundation model for fine-grained robot manipulation. *arXiv preprint arXiv:2607.04927*, 2026.

Lifeng Zhuo, Wendi Chen, Han Xue, Shirun Tang, Jun Lv, Cewu Lu, and Chuan Wen. Fa-rdp: A frequency-adaptive reactive diffusion policy for contact-rich manipulation. *arXiv preprint arXiv:2607.28596*, 2026.

APPENDIX

A Action Foundation Model **16**

B Module Implementation **16**

B.1 Visual Memory Retrieval 16

B.2 Tactile Encoding 17

B.3 Residual Editing 17

C Learning Details **18**

C.1 Loss Function 18

C.2 Predictive Conditions 19

C.3 Training Strategy 19

D Action and Evaluation Conventions **19**

D.1 Action Layout and Temporal Alignment 19

D.2 Evaluation Masks and Aggregation 20

E Visual-Only Action Prediction **21**

F Real-Robot Setup and Demonstration Collection **21**

G Additional Qualitative Results **22**

G.1 Additional EgoTouch Qualitative Examples 22

G.2 Additional Tachin Qualitative Examples 24

G.3 Additional Real-Robot Qualitative Examples 26

A Action Foundation Model

General-purpose manipulation policies increasingly adapt large pretrained backbones to action prediction (Wu et al., 2026a; Ye et al., 2026a; Yuan et al., 2026; Black et al., 2024b; Pertsch et al., 2025; Kim et al., 2025; Team et al., 2024; Liu et al., 2025a; Bjorck et al., 2025; Team et al., 2025; Shukor et al., 2025; O'Neill et al., 2024; Driess et al., 2023; Brohan et al., 2022; Reed et al., 2022). Vision–language–action (VLA) models follow this approach by predicting robot commands from visual observations and language instructions. RT-2 (Brohan et al., 2023) represents actions as tokens to jointly train on robot trajectories and web data, while OpenVLA (Kim et al., 2024) fine-tunes a pretrained vision–language backbone on a large collection of real robot demonstrations. More recent work expands the data and supervision available for policy learning. $\pi_{0.5}$ (Physical Intelligence et al., 2025) combines robot trajectories, web data, and subtask supervision to support generalization to unseen environments. SmolVLA (Shukor et al., 2025) emphasizes efficient training with community demonstrations, while VITRA (Li et al., 2025) learns a hand-motion prior from human activity videos. World–action models (WAMs) (Hou et al., 2026) further incorporate future-state prediction to learn representations of how the environment evolves. FLARE (Zheng et al., 2025) predict future observation embeddings rather than reconstructing future pixels. Dream-zero Ye et al. (2026b) jointly predict future video and robot actions. Fast-WAM (Yuan et al., 2026) use predictive learning during training while removing the predictor at deployment. These methods motivate learning control representations through future prediction. However, they run on single clock: visual observations, learned representations, and action predictions are updated together. In contact-rich manipulation, this coupling is restrictive because local contact conditions can change faster than the visual policy is updated. In these situations, a further challenge is to make these representations useful for tactile corrections between visual updates. T-WLA addresses this challenge by caching a history-aware visual representation that a faster tactile controller can reuse.

B Module Implementation

This appendix expands the implementation of the operators introduced in the main text. We retain M_{V}^{t} for the final visual memory, $Z_{t,\tau}$ for the reference-centered tactile context, and $\Delta A_{t,\tau}$ for the effective action correction. Numerical specifications below refer to the reference implementation; the contact-filtered variant is identified where it changes an operation or its valid supervision set.

B.1 Visual Memory Retrieval

Queries, reference slots, and historical tokens. Let t denote the current visual update. The retrieval module has $S = 8$ learned query tokens $Q_{\mathrm{V}} = [Q_{\mathrm{V},1}, \ldots, Q_{\mathrm{V},S}] \in \mathbb{R}^{S\times d}$, each of width $d = 960$. Its history bank stores up to $K = 8$ previous visual output-memory sets $M_{\mathrm{V}}^{t-k} \in \mathbb{R}^{S\times d}$, where $k = 1$ denotes the most recent set. For slot $j \in 1, \ldots, S$, $e_j^{\mathrm{slot}} \in \mathbb{R}^d$ identifies the slot; for age $k \in 1, \ldots, K$, $e_k^{\mathrm{age}} \in \mathbb{R}^d$ identifies how many visual updates ago the set was produced. The query stream starts from Q_{V}, while the key/value stream contains learned reference slots and available historical tokens:

$$r_j = Q_{\mathrm{V},j} + e_j^{\mathrm{slot}}, \tag{4}$$

$$b_{k,j}^{t} = M_{\mathrm{V},j}^{t-k} + e_j^{\mathrm{slot}} + e_k^{\mathrm{age}}, \qquad k \in \{1, \ldots, K\}. \tag{5}$$

Thus, r_j is the reference token for slot j, reusing the query parameter rather than introducing a separate learned vector; $b_{k,j}^{t}$ is the token from slot j of the output memory written k visual updates earlier. Queries attend to all reference tokens and valid historical tokens; unavailable history is masked. Slot and age embeddings are added only during retrieval and are not stored in the bank. Age is measured in visual updates, not tactile events or action-flow steps.

Masking and output extraction. Unused bank positions are zeroed and excluded by the attention mask; reference slots remain valid even when the bank is empty. Two retrieval blocks use pre-normalized cross-attention and SwiGLU feed-forward layers, with 15 attention heads and an intermediate width of 2560. The blocks use Q/K RMS normalization, a learned attention-logit scale, and zero-initialized $\tanh$ gates on their residual branches. The retrieved input memory is placed after the image, field-of-view, language, and state tokens in the visual backbone input. The final M_{V}^{t} is read

directly from the last decoder layer at these eight memory positions, without an additional readout projection. The bank stores this observation-contextualized output, not the retrieved input memory. Episode boundaries reset the bank; a visual event writes one new memory set, independently of the number of action-flow integration steps.

B.2 TACTILE ENCODING

Sensor processing and temporal encoding. Each hand is represented by its eight most recent causally available 21×21 pressure maps. Invalid temporal observations are zeroed, and the left-hand maps are flipped along the spatial horizontal axis to establish a common hand convention. Pressure and the spatial sensor-validity mask form two input channels. A shared CNN uses three 5×5 convolutional layers with 32 channels, padding 2, ReLU activations, and 2×2 max-pooling. The resulting 128-dimensional frame features enter a two-layer bidirectional GRU with hidden width 120 per direction. The final forward and initial backward states are concatenated and projected from 240 to 64 dimensions, followed by ℓ_2 normalization. Both GRU directions operate within the observed history window; neither accesses a future tactile frame.

Reference subtraction.

Let F_{T} denote the shared tactile encoder, including its output normalization but excluding reference subtraction. At tactile update (t, τ), $\mathcal{H}^r_{t,\tau}$ is the ordered tactile history for hand $r \in \{\mathrm{L}, \mathrm{R}\}$, and $\mathcal{H}^r_{\mathrm{ref}}$ is its fixed, hand-specific reference history. Both are encoded with the same module F_{T}. The reference-centered representation supplied to the tactile editor is

$$Z^r_{t,\tau} = v^r_{t,\tau} \left[F_{\mathrm{T}}(\mathcal{H}^r_{t,\tau}) - F_{\mathrm{T}}(\mathcal{H}^r_{\mathrm{ref}}) \right]. \tag{6}$$

Here $v^r_{t,\tau} \in \{0, 1\}$ equals one only when the encoded history passes its validity check and the most recent tactile observation is valid; otherwise, the representation is set to zero. In the contact-filtered variant, contact validity additionally affects the temporal mask used to encode the history, rather than introducing a separate gate after subtraction. Each encoder output is normalized before subtraction; the resulting difference is not normalized again.

The fixed reference is a raw pressure window, not a cached embedding. Actual and reference windows are concatenated along the batch dimension, encoded together on every forward pass, and separated before subtraction. Consequently, both encoding paths receive gradients when the encoder is trained. The reference-statistics routine pools valid training pressure observations from history windows and the associated future-pressure targets, and repeats the per-taxel mean across the eight reference frames. These are fixed training-set statistics, not sample-specific future inputs to the controller. The exact statistics asset belongs to the training configuration.

B.3 RESIDUAL EDITING

Action features and tactile modulation. The editor maps the visual memory and base-action tokens to width 256. Visual tokens use RMS normalization followed by a bias-free projection; base-action tokens are standardized for their input projection. Modality, action-position, and elapsed-time embeddings distinguish the token roles. The elapsed-time projection receives $10\Delta t_{t,\tau}$, with elapsed time expressed in seconds. A two-layer pre-normalized Transformer uses eight heads, a feed-forward width of 1024, GELU activations, and zero dropout. Only its action-position outputs, denoted H_{act}, enter the residual readout.

For each hand, a bias-free linear map from its 64-dimensional tactile context produces the FiLM scale and shift. Here Z^r abbreviates the reference-centered context $Z^r_{t,\tau}$ defined above, and H_{act} denotes the action features associated with the active base chunk. The scale and shift have dimensions compatible with H_{act}, allowing each hand's tactile context to modulate these action features before readout. With U^r denoting an internal, unmasked correction, the readout is

$$U^r = W^r_{\mathrm{out}}[\gamma^r(Z^r) \odot H_{\mathrm{act}} + \beta^r(Z^r)], \tag{7}$$

$$\Delta A_{t,\tau} = \sum_{r \in \{\mathrm{L},\mathrm{R}\}} m^r_{\mathrm{edit}} \odot U^r. \tag{8}$$

Here $\odot$ denotes element-wise multiplication. Each output projection W^r_{out} maps the modulated features to action coordinates; it is bias-free and zero-initialized so that training starts with zero

correction. The mask m^r_{edit} intersects the editable action positions, that hand's component mask, and hand validity. Thus $\Delta A_{t,\tau}$ retains its main-text meaning as the effective correction added to the cached base chunk, rather than the raw network output. Every update is relative to the same base chunk, not to a previously corrected chunk.

Causal contact gate. The contact-filtered variant uses a hard gate computed from observed pressure history. Let $P_{j,r}$ be the pressure map of hand r at history index j, let $\mathcal{S}_r$ contain its valid sensor sites, and let $\mathcal{J}_r$ contain its valid history indices. The gate is

$$c^r = \mathbf{1}\left[\max_{j\in\mathcal{J}_r} \frac{1}{5} \sum_{u\in \text{Top5}(P_{j,r}|_{\mathcal{S}_r})} P_{j,r,u} \geq \eta\right], \qquad \eta = 0.25. \tag{9}$$

Here Top5 returns the indices of the five largest valid pressure values. An empty valid history gives $c^r = 0$. The reference threshold is expressed in the input pressure scale. The gate detects whether a valid history frame crosses the threshold; it does not require contact at the latest frame and is not learned from future contact labels.

The same c^r is intersected with the hand's temporal tactile-validity mask, action-supervision mask, and future-pressure-validity mask. A gated-out hand therefore receives zero correction and retains its base action, but its excluded action entries are not counted as zero-error observations in the loss. The contact wrapper does not directly change the RGB target validity mask. Sample-level contact filtering and its evaluation denominator are described in Appendix D.2.

C Learning Details

C.1 Loss Function

Visual action loss. The group-balanced operators for the visual expert and the tactile editor have different reduction orders. Let b, j, and d index a minibatch sample, an action position, and an action component. For visual velocity error $e_{b,j,d}$, validity mask $m^{\text{V}}_{b,j,d}$, and component group $\mathcal{D}_g$, define

$$n_g = \sum_{b,j}\sum_{d\in\mathcal{D}_g} m^{\text{V}}_{b,j,d}, \qquad \ell_g = \frac{\sum_{b,j}\sum_{d\in\mathcal{D}_g} m^{\text{V}}_{b,j,d} e^2_{b,j,d}}{n_g}, \tag{10}$$

$$\mathcal{L}^{\text{V}}_{\text{act}} = \frac{\sum_{g:n_g>0} w_g \ell_g}{\sum_{g:n_g>0} w_g}. \tag{11}$$

Here ℓ_g is defined only for $n_g > 0$; a minibatch with no valid groups contributes zero loss. The within-group mean is formed over the entire minibatch, not separately for each sample. Empty groups are excluded. The reference configuration uses equal group weights and no additional horizon weighting.

Edited-action loss and residual penalty. Let b, j, and d index a minibatch sample, an action position, and an action component, respectively, and let $\mathcal{D}_g$ be the components in group g. For corrected-action error $e_{b,j,d} = \widehat{A}_{b,j,d} - A^\star_{b,j,d}$, where $\widehat{A}$ is the corrected action chunk and $A^\star$ is the demonstration chunk, let $m^{\mathcal{E}}_{b,j,d}$ denote the effective valid, editable supervision mask and $n_{b,g} = \sum_j \sum_{d\in\mathcal{D}_g} m^{\mathcal{E}}_{b,j,d}$ the number of supervised entries in group g for sample b. Write $\mathcal{G}_b = \{g : n_{b,g} > 0\}$ for the nonempty groups in sample b and $\mathcal{B}_+ = \{b : |\mathcal{G}_b| > 0\}$ for the supervised samples. The minibatch estimator is

$$\mathcal{L}_{\text{edit}} = \frac{1}{|\mathcal{B}_+|}\sum_{b\in\mathcal{B}_+} \frac{1}{|\mathcal{G}_b|}\sum_{g\in\mathcal{G}_b} \frac{\sum_j\sum_{d\in\mathcal{D}_g} m^{\mathcal{E}}_{b,j,d}\rho(e_{b,j,d})}{n_{b,g}}, \tag{12}$$

where $\rho(e) = \frac{1}{2}e^2$ for $|e| < 1$ and $\rho(e) = |e| - \frac{1}{2}$ otherwise. Thus the editor averages nonempty groups within each sample before averaging supervised samples. Invalid targets are replaced safely before elementwise evaluation so that invalid entries do not introduce non-finite losses.

In contrast, the residual penalty is a single mean over all effective action entries:

$$\widehat{\mathcal{R}}_\Delta = \frac{\sum_{b,j,d} m^{\mathcal{E}}_{b,j,d}(\Delta A_{b,j,d})^2}{\sum_{b,j,d} m^{\mathcal{E}}_{b,j,d}}, \tag{13}$$

where $\Delta A_{b,j,d}$ is the effective residual added to the base action at that entry. It does not rebalance groups or hands. When $\mathcal{B}_+$ is empty, or when the residual penalty has no valid entries, the corresponding loss is defined as zero. Contact filtering changes the valid sets in both expressions, rather than adding artificial zero-loss examples.

C.2 Predictive Conditions

Tactile-conditioned visual prediction. During tactile editor training, a learned adapter maps the tactile context $Z_{t,\tau}$ to an additive update of the eight visual-memory tokens used by the frozen visual predictor. This update affects only the prediction condition; the cached visual memory used for action generation remains unchanged. Let y denote the clean future-image latent, ε the sampled Gaussian noise, and v_Z the predictor's velocity under the tactile-augmented condition. We supervise v_Z with the conditional flow-matching target $\varepsilon - y$. Although the implementation expresses this objective relative to the unaugmented prediction, the resulting loss is algebraically identical to the conditional flow-matching loss. The predictor's parameters are frozen, but gradients through its tactile-augmented forward pass update the adapter and tactile encoder. The squared error is spatially weighted, normalized by the weighted valid element count for each sample–horizon pair, and averaged over valid pairs. Reference ROI weights are 1 for the hand region and 0.1 for the background.

Future-pressure prediction. The pressure predictor uses detached cached visual memory, tactile context, and a detached window of upcoming edited actions generated by the controller to predict future pressure. Detaching the action window prevents this loss from sending gradients through the action condition into the residual readout, while gradients through the tactile context can update the shared tactile encoder. The target is measured future pressure, not a learned tactile embedding. For hand $r \in \{\mathrm{L}, \mathrm{R}\}$ and pressure site $u \in \{1, \ldots, 441\}$, a fixed codec canonicalizes hand orientation and standardizes the future pressure $P_u^{+,r}$ using the corresponding training-set mean μ_u^r and standard deviation σ_u^r:

$$y_u^r = \frac{P_u^{+,r} - \mu_u^r}{\max(\sigma_u^r, 10^{-3})}. \tag{14}$$

Future-hand validity and spatial sensor masks select the sites included in the flow-matching loss, which is averaged over all valid sites rather than weighting the two hands equally. In the contact-filtered variant, the future-hand mask also includes the gate computed from current tactile history; no gate is computed from the future target. The reference predictor uses four Transformer decoder layers of width 256 with eight attention heads.

C.3 Training Strategy

For tactile pretraining, synchronized tactile and hand-pose histories from EgoTouch are encoded into normalized embeddings u_i and p_i, with tactile embeddings taken before reference subtraction. Their similarities are computed as $S_{ij} = \alpha u_i^\top p_j$, where $\alpha > 0$ is a learned scale. The symmetric contrastive objective averages row-wise cross-entropy over S and $S^\top$, treating synchronized pairs as positives and other pairs in the minibatch as negatives. During editor training, the visual branch supplies cached visual memory and base action chunks and remains frozen. The tactile encoder, residual editor, tactile conditioning adapter, and pressure predictor are updated, while the visual predictor remains frozen. As a proposed extension, both control branches could be jointly fine-tuned on EgoTouch using the same action and predictive objectives. In this stage, visual memory and base action chunks would be recomputed online, allowing the corrected-action loss to also update the visual branch through the memory interface. The visual predictor would remain frozen.

D Action and Evaluation Conventions

D.1 Action Layout and Temporal Alignment

Action coordinates. The hand-motion interface uses $H = 16$ action positions and 192 channels per position. Of these, 138 channels contain motion data and 54 are padding. Table 4 gives the component groups used by the losses. Padding is excluded from supervision and from valid sampled action components; it is not an additional action degree of freedom.

Table 4: Hand-motion action layout. Indices are zero-based, half-open intervals. Joint channels store 21 three-dimensional local positions per hand.

Component	Left hand	Right hand	Channels per hand
Wrist translation increment	$[0, 3)$	$[69, 72)$	3
Wrist Euler rotation increment	$[3, 6)$	$[72, 75)$	3
Palm-local joint coordinates	$[6, 69)$	$[75, 138)$	63
Padding	$[138, 192)$		—

Table 5: Visual-only future hand-motion prediction. GigaHands uses its five official activity families; OakInk2 and TACO use their complete held-out test sets. The GigaHands average gives equal weight to the five families. Lower prediction error is better. Gray highlights T-WLA. **Bold**/underline indicate the best/second-best distinct reported errors within each metric and column, including ties. Frequency is reported in Hz and is not ranked. Dashes indicate unavailable results and are excluded from ranking.

	GigaHands						OakInk2	TACO	
Method	Cook.	Office	Craft.	Entert.	Housew.	Avg.	Overall	Overall	Freq.
Wrist translation error (cm, ↓)									
VITRA	1.16	1.25	1.11	1.44	1.37	1.27	0.53	0.97	19.4
SmolVLA	0.84	0.81	0.73	1.01	0.98	0.87	0.50	**0.72**	23.0
MemoryVLA	1.32	1.26	1.23	1.35	1.35	1.30	1.05	1.20	8.8
T-WLA	**0.63**	**0.60**	**0.56**	**0.69**	**0.74**	**0.65**	**0.44**	0.75	39.7
Wrist rotation geodesic error (degrees, ↓)									
VITRA	5.32	5.79	5.13	6.72	7.00	5.99	2.03	4.76	19.4
SmolVLA	3.75	3.91	3.69	5.07	5.23	4.33	2.03	3.68	23.0
MemoryVLA	6.52	6.54	6.07	6.97	7.25	6.67	5.27	6.66	8.8
T-WLA	**3.19**	**3.41**	**3.13**	**4.01**	**4.45**	**3.64**	**1.38**	**3.40**	39.7
Wrist-relative finger-joint MPJPE (cm, ↓)									
VITRA	1.48	1.32	1.36	1.41	1.36	1.39	2.04	2.74	19.4
SmolVLA	0.96	0.94	0.94	0.95	0.95	0.95	1.13	1.03	23.0
MemoryVLA	4.00	3.91	3.78	3.90	3.99	3.92	3.92	4.02	8.8
T-WLA	**0.43**	**0.43**	**0.41**	**0.44**	**0.45**	**0.43**	**0.37**	**0.46**	39.7

Chunk positions and auxiliary action windows. The visual branch and tactile editor operate at 39.7 Hz and 119.1 Hz, respectively. Each visual update produces a new base action chunk. Between visual updates, the tactile editor uses incoming tactile observations to revise the unexecuted actions in the active chunk. The elapsed time $\Delta t_{t,\tau}$ is measured from the start of that chunk rather than inferred from the tactile update index.

For future-pressure conditioning, the action window begins at $k_0 = \lceil f_{\mathrm{cmd}} \Delta t_{t,\tau} \rceil$, where f_{cmd} is the action command rate, and contains the next eight edited actions. A floating-point tolerance is applied at integer boundaries. Positions beyond the chunk are zero-padded and marked invalid. This auxiliary window-indexing rule is distinct from the loss horizon and from the temporal mask that marks already executed actions as non-editable.

D.2 Evaluation Masks and Aggregation

Physical hand-motion errors. The hand-motion evaluator supports a declared horizon H_{eval} of eight or sixteen positions. A hand is eligible only if its complete evaluated prefix is valid; a truncated prefix is not silently substituted for the declared horizon. Predictions and targets are compared in the physical action coordinates used by the evaluator.

At prediction step k, wrist translation increments are accumulated from the start of the prediction window before computing the Euclidean error in centimeters. Euler rotation increments are converted using the xyz convention and composed by left multiplication, $R_k = \delta R_k R_{k-1}$ with $R_0 = I$;

predicted rotations are composed in the same way. The resulting rotational error, in degrees, is

$$e_{\mathrm{rot}}(R, \widehat{R}) = \frac{180}{\pi} \arccos\left(\mathrm{clip}_{[-1,1]}\left(\frac{\mathrm{tr}(\widehat{R}^{\top} R) - 1}{2} \right) \right). \tag{15}$$

Finger-joint MPJPE compares the stored palm-local positions directly, averaging joints 1–20 and reporting centimeters. Joint 0 is the fixed local origin and is excluded; the evaluator does not subtract a predicted wrist position from already local joint coordinates.

Sequence-level aggregation. For each metric, errors are first summed over eligible hand–time entries within each sequence and divided by their valid count. Sequences with no eligible entries are excluded. Environment-level means then weight these sequence means equally. The EgoTouch macro-average gives equal weight to its five environment means; the Tachin overall score gives equal weight to its eligible sequence means. This aggregation differs from pooling all frames and should not be replaced by a sample-weighted mean from a different evaluation entry point.

Contact-conditioned evaluation. In the contact-filtered protocol, a sample is admitted when at least one supervised hand satisfies the causal gate in Eq. 9. Per-hand masks then exclude noncontact hands from action and future-pressure supervision. These exclusions define a contact-conditioned subset of the held-out data, not the complete held-out test set. Retaining the base action for an excluded hand does not insert that hand into the metric denominator. Comparisons under this protocol require a common sample set, hand mask, and prediction horizon; results on an unfiltered test set represent a separate evaluation protocol.

E Visual-Only Action Prediction

The visual-only experiment evaluates future hand-motion prediction when touch is unavailable. Tactile observations are excluded during both training and evaluation, and tactile supervision is disabled during training. The model uses only RGB, language, pose history, recurrent visual memory, and the visual action expert. Thus,

$$a = a^{\mathrm{base}}, \qquad \mathcal{L}_{\text{visual-only}} = \mathcal{L}_{\mathrm{act}} + \lambda_{\mathrm{vis}} \mathcal{L}_{\mathrm{vis}}. \tag{16}$$

This setting isolates the visual pathway rather than testing cross-modal transfer.

Table 5 shows that T-WLA remains competitive without touch and achieves the best completed result on eight of the nine dataset-level metric comparisons. On GigaHands, T-WLA obtains average translation, rotation, and joint errors of 0.65 cm, $3.64°$, and 0.43 cm. Relative to SmolVLA, these values correspond to reductions of 25.3%, 15.9%, and 54.7%, respectively. The improvement is consistent across all five activity families rather than being concentrated in a single category.

On OakInk2, T-WLA reaches 0.44 cm translation error, $1.38°$ rotation error, and 0.37 cm joint MPJPE, reducing the corresponding SmolVLA errors by 12.0%, 32.0%, and 67.3%. On TACO, T-WLA achieves the lowest completed rotation and joint errors at $3.40°$ and 0.46 cm, improving over SmolVLA by 7.6% and 55.3%. Its translation error is 0.75 cm, slightly above SmolVLA's 0.72 cm but still 22.7% below VITRA. These results show that separating tactile correction from visual action generation does not weaken the visual predictor; instead, the visual memory and predictive supervision provide a strong action prior even when the tactile branch is absent.

F Real-Robot Setup and Demonstration Collection

Hardware. Our platform is a dual-arm Linker A7black robot with a 7-DoF arm and a Linker Hand L6 dexterous hand on each side. The hands provide fingertip tactile sensing. We mounted an Intel RealSense D435i on a custom 3D-printed bracket to capture an egocentric view of the workspace and calibrated its pose relative to the robot.

Teleoperation. An operator wears Wuji data gloves to capture finger articulation and HTC VIVE Tracker 3.0 devices at the wrists to track wrist motion. Two SteamVR Base Station 2.0 units track the VIVE devices. The tracked wrist poses and glove measurements are mapped to the robot arms and dexterous hands to collect task demonstrations; no VR headset is required.

Demonstration budget. We collect 30 teleoperated episodes for each of the four real-robot tasks: egg handling, single-sheet pickup, paper-cup nesting, and paper-bag opening.



(a) Rrobot hardware platform (b) Data glove

Figure 6: **Robot platform and data glove**

G Additional Qualitative Results

We provide additional qualitative comparisons on EgoTouch and Tachin to complement the examples shown in Fig. 4. Throughout this section, VITRA, SmolVLA, MemoryVLA, and T-Rex refer to their tactile-augmented variants used in Table 1, whereas T-WLA uses its native tactile-conditioned interface. We follow the same visualization protocol as Fig. 4. For each example, the source RGB observation is shown at t_0, while the ground-truth pose and all model predictions correspond to $t_0 + 100\,\mathrm{ms}$. Camera-frame overlays visualize the complete predicted hand pose, whereas wrist-aligned views emphasize differences in finger articulation. The value below each prediction is the per-example wrist-aligned MPJPE over the 20 non-root hand joints at $t_0 + 100\,\mathrm{ms}$. These values are intended only as diagnostics for the displayed examples and should not be interpreted as dataset-level test averages. They isolate finger-articulation error after wrist alignment and are therefore distinct from the wrist-translation and wrist-rotation metrics reported in Table 1. Across the displayed examples, T-WLA consistently produces fingertip configurations that more closely match the ground truth and achieves the lowest per-example wrist-aligned MPJPE among the compared methods. This mirrors the quantitative results in Table 1: the largest gains from T-WLA occur in finger-joint MPJPE, substantially exceeding the relative improvements in wrist translation and rotation. Together, these results suggest that T-WLA is particularly effective at predicting fine-grained fingertip and finger-articulation dynamics.

G.1 Additional EgoTouch Qualitative Examples

Figures 7 and 8 show six additional EgoTouch examples. We first visualize predictions in the camera frame and then use wrist-aligned renderings to isolate differences in finger articulation.



Figure 7: **Additional camera-frame qualitative comparisons on EgoTouch.** Each row shows the source RGB observation at t_0, followed by the ground-truth hand pose and predictions from VITRA, SmolVLA, MemoryVLA, T-Rex, and T-WLA at $t_0 + 100\,\mathrm{ms}$. Ground truth is shown in green and model predictions in orange. Values below each prediction report the corresponding wrist-aligned finger-joint MPJPE in centimeters.

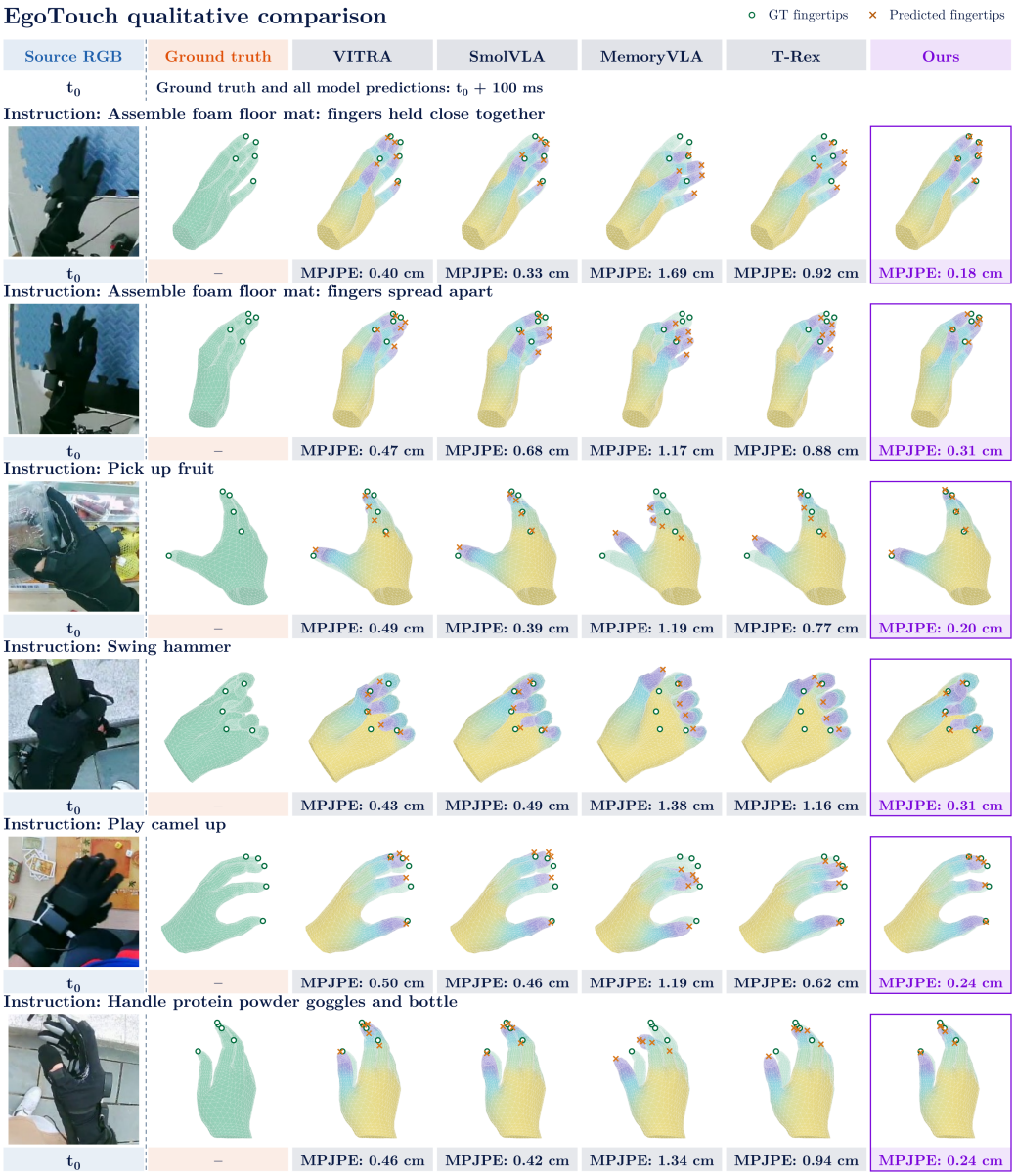


Figure 8: **Additional wrist-aligned fingertip comparisons on EgoTouch.** The same six examples from Fig. 7 are shown after wrist alignment to emphasize finger articulation independently of global wrist motion. Within each example, all hands share the same alignment, scale, and $+60°$ visualization rotation. The ground-truth hand mesh is shown in green, with ground-truth fingertips marked by green circles and predicted fingertips marked by orange crosses. Values below each prediction report wrist-aligned MPJPE over the 20 non-root hand joints at $t_0 + 100\,\mathrm{ms}$. These values are per-example diagnostics rather than dataset-level test averages.

G.2 Additional Tachin Qualitative Examples

Figures 9 and 10 show six additional Tachin examples covering diverse hand orientations and finger configurations. We first visualize the future hand-pose predictions directly in the camera frame, where the source RGB observation is shown at t_0 and the ground-truth and predicted poses correspond to $t_0 + 100\,\mathrm{ms}$. This view preserves both global wrist motion and finger articulation, allowing direct comparison of the complete predicted hand pose.

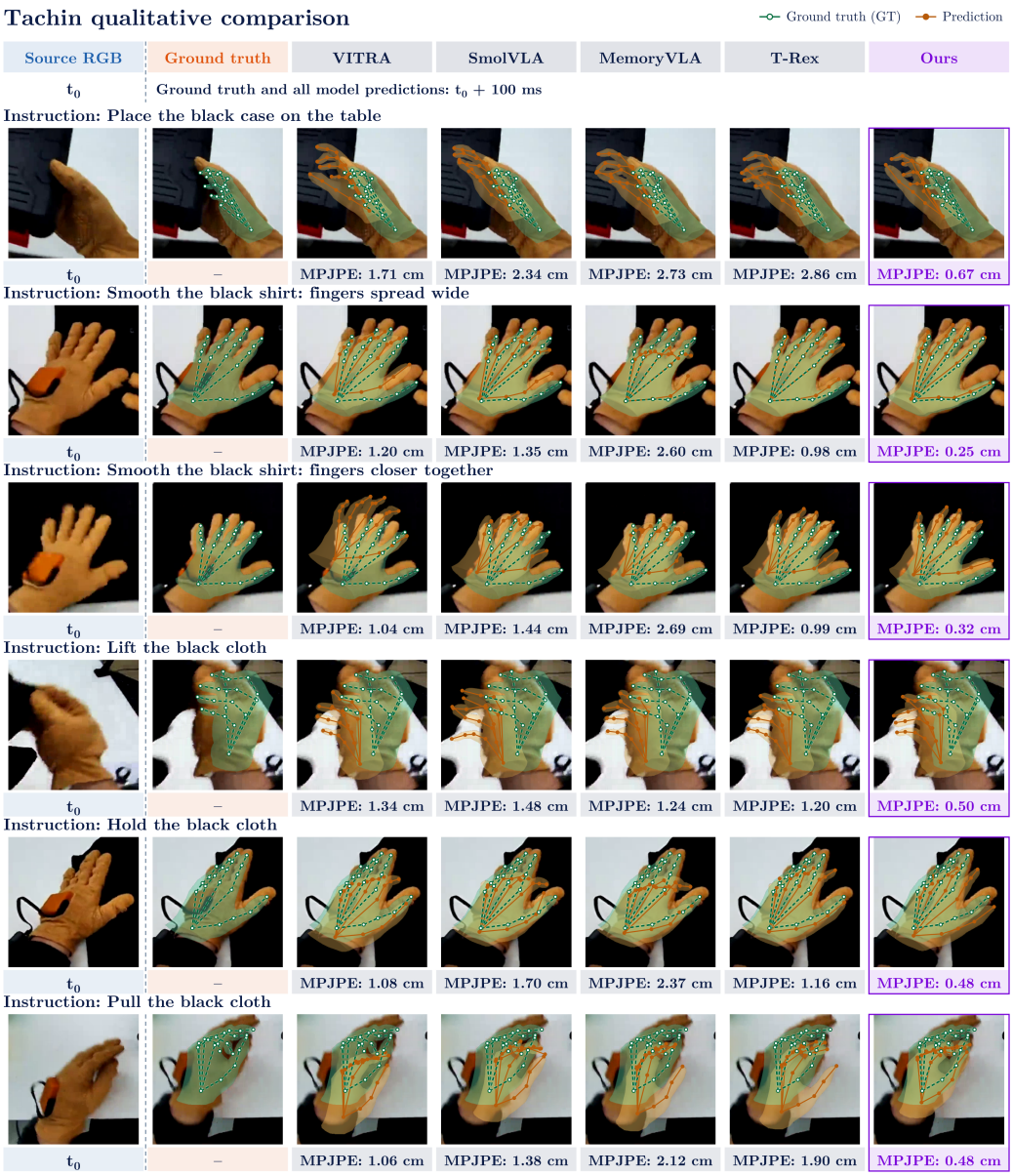


Figure 9: **Additional camera-frame qualitative comparisons on Tachin.** Each row shows one source RGB observation at t_0, followed by the ground-truth hand pose and predictions from VITRA, SmolVLA, MemoryVLA, T-Rex, and T-WLA at $t_0 + 100\,\mathrm{ms}$. Ground-truth hand poses are shown in green and model predictions in orange. This camera-frame visualization preserves both global wrist motion and finger articulation. The values below each prediction report the corresponding wrist-aligned finger-joint MPJPE in centimeters.

We then show wrist-aligned fingertip-detail renderings for the same examples. Removing global wrist displacement makes differences in finger articulation easier to inspect independently of the hand's position in the camera frame. Across the displayed examples, T-WLA more closely matches the ground-truth fingertip configuration and achieves the lowest per-example wrist-aligned MPJPE in every row. These qualitative examples complement the dataset-level quantitative results reported in Table 1.

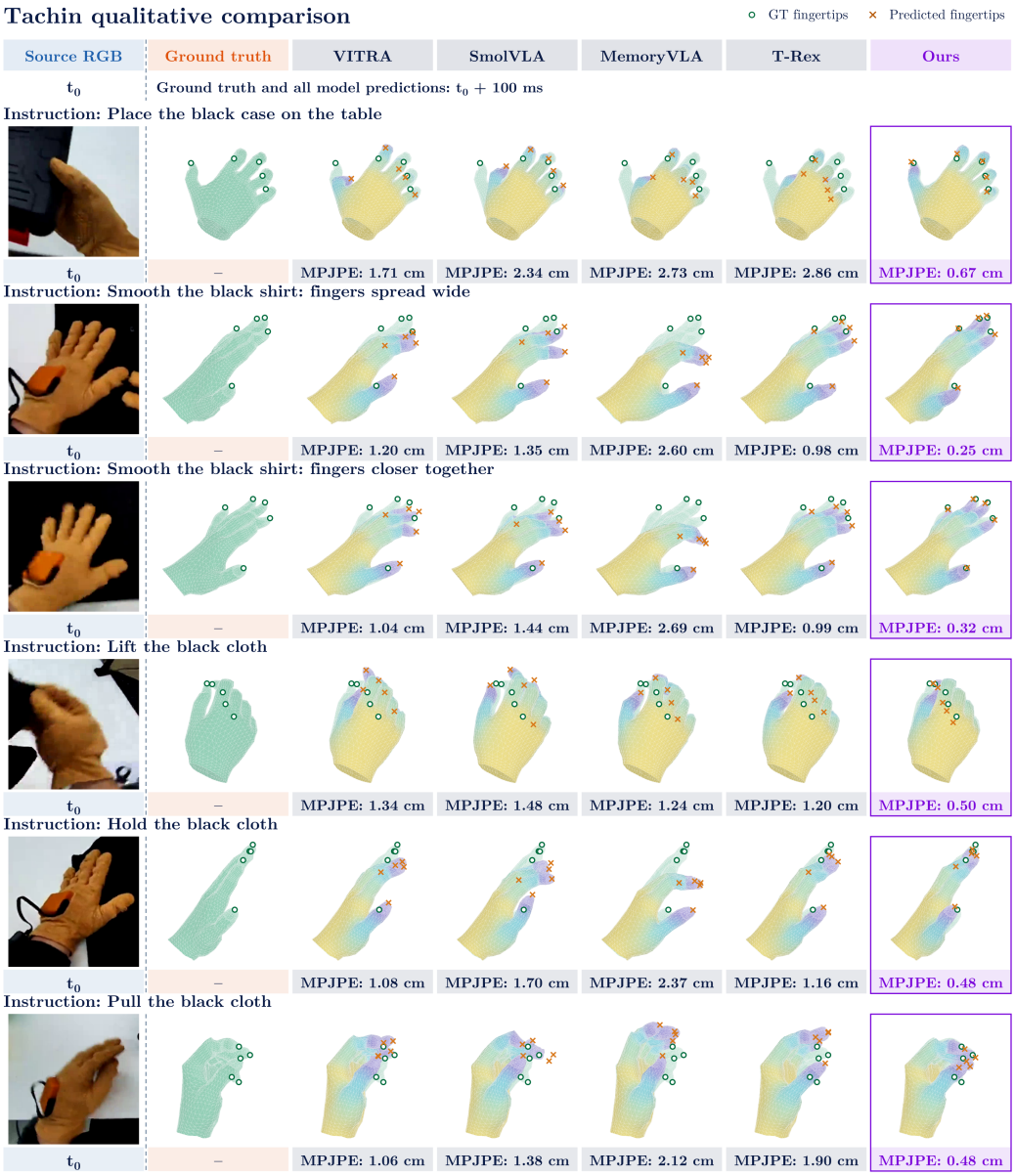


Figure 10: **Additional wrist-aligned fingertip comparisons on Tachin.** The same six examples from Fig. 9 are shown after wrist alignment to emphasize finger articulation independently of global wrist motion. Within each example, all hands share the same alignment, scale, and $+60°$ visualization rotation. The ground-truth hand mesh is shown in green, with ground-truth fingertips marked by green circles and predicted fingertips marked by orange crosses. Values below each prediction report wrist-aligned MPJPE over the 20 non-root hand joints at $t_0 + 100\,\mathrm{ms}$. These values are per-example diagnostics rather than dataset-level test averages.

G.3 Additional Real-Robot Qualitative Examples

Figure 11 presents additional real-robot examples of paper-bag dragging and single-sheet pickup. Both tasks require precise contact with a thin edge, but impose different demands after grasping: sheet pickup requires maintaining a secure pinch without crumpling the paper, whereas dragging a loaded bag requires sustaining the grasp under changing fingertip loads. Tactile feedback provides

contact information relevant to these adjustments, complementing visual guidance. These examples supplement the closed-loop success rates reported in Table 2.

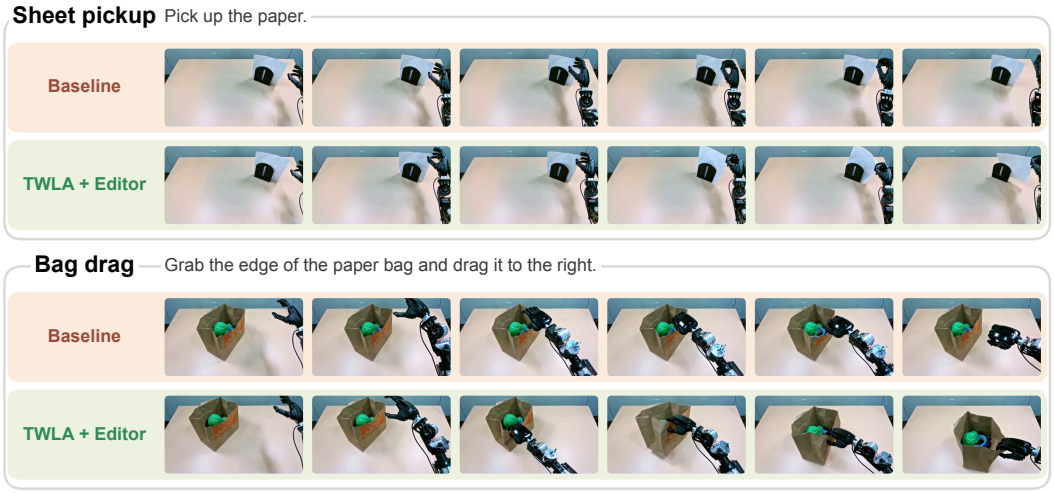


Figure 11: **Additional real-robot qualitative examples.** Selected frames from paper-bag dragging and single-sheet pickup. Both tasks involve grasping thin, deformable edges, requiring sustained contact during dragging or a delicate pinch during lifting.